Determination of optical scattering properties in turbid media using Mueller matrix imaging

Brent D. Cameron
Yanfang Li
Ajaina Nezhuvingal
University of Toledo
Department of Bioengineering
Toledo, Ohio 43606-3390

Abstract. A need exists for the continued development of diagnostic tools and methods capable of distinguishing and characterizing slight differences in the optical properties of tissues. We present a method to estimate the scattering coefficient contribution as a function of particle size in complex mixtures of polystyrene spheres. The experimental method we used is a Mueller matrix imaging approach. The Mueller matrix encodes the polarization-dependent properties of the sample and describes how a given sample will transform an incident light polarization state. A partial least-squares approach is used to form a model around a set of Mueller matrix image-based measurements to accurately predict the individual scattering coefficient contributions in phantoms containing 0.2, 0.5, 1, and 2 μm-diameter polystyrene spheres. The results show individual scattering coefficient contribution errors as low as 0.1585 cm^{-1} can be achieved. In addition, it is shown how the scattering type (i.e., Rayleigh and Mie) is encoded within the Mueller matrix. Such methods may eventually lead to the development of improved diagnostic tools capable of characterizing and distinguishing between tissue abnormalities, such as superficial cancerous lesions from their benign counterparts. © *2006 Society of Photo-Optical Instrumentation Engineers.* [DOI: 10.1117/1.2363347]

Keywords: Mueller matrix; polarization; scattering; partial least squares.

1 Introduction

It is well known that through the characterization of the polarization effects in scattered light, useful information on the properties of turbid media can be obtained. As early as 1976, Bickel et al. found that *Bacillus Subtilis* suspensions affected the angular distributions of the scattering matrix.[1] Expanding on this early work, Hielscher et al. investigated how radial and azimuthal variations observed in diffusely backscattered polarization images of intralipid and polystyrene sphere suspensions changed with particle size, concentration, and the anisotropy factor.[2] Backman et al.[3] and Bartlett et al.[4] also demonstrated how polarized light scattering spectroscopy can be used to measure and characterize particle size distribution. In regards to *in vivo* tissue characterization, Demos et al.[5] and Jacques et al.[6] also reported on the use of backscattered polarized light for surface and subsurface imaging of biological materials. In these investigations, it was found that through the use of polarized light, the contrast of polarization-sensitive structures in tissue could be significantly enhanced to provide useful diagnostic information. Most recently, in 2004, Yaroslavsky et al.[7] demonstrated how polarization-based reflectance and fluorescence imaging can be used for improved demarcation of skin tumors, and in 2005, Angelsky et al.[8] investigated how the correlation structure of biological tissue polarization images can be used for cancer diagnostics. These investigations represent only a brief subset of the numerous and considerable advances in polarization-based biological measurements made over the past few years.

When describing photon migration in turbid media, common parameters of interest are the absorption coefficient, μ_a, the scattering coefficient, μ_s, and the scattering phase function. Although several methods may be used to experimentally measure these parameters, the inverse adding-doubling integrating sphere technique is a popular approach.[9] Other useful optical parameters can also be experimentally measured by other approaches, such as by the method reported by Wang et al.[10] In their investigation, a laser beam with an oblique angle of incidence was used to measure the reduced scattering coefficient of turbid media. Bevilacqua et al.[11–13] also reported on local and superficial optical characterization of biological tissues achieved through spatially resolved diffuse reflectance at small source-detector separations. In these works, they investigated how extremely sensitive the determination of the absorption and reduced scattering coefficients are in relation to the phase function. However, regardless of the technique, most optical property measurement approaches only take into account the overall optical properties of the sample. In this paper, we present a technique to quantify the individual optical scattering coefficient contributions as a function of particle size for complex mixtures of polystyrene

Address all correspondence to Brent Cameron, Bioengineering, Univ. of Toledo, 5030 Nitschke Hall - 2801 W. Bancroft Street, Toledo, OH 43606-3390, United States of America. Tel: 419-530-8277; Fax: 360-397-6713; E-mail: bcameron@eng.utoledo.edu

spheres. This technique exploits information encoded in the polarization-sensitive Mueller matrix, which is well known to provide a complete description of the polarization properties of an optical sample.[14–16] In order to predict the scattering coefficient contribution for an individual particle size in complex suspensions consisting of a mixture of particle sizes, a partial least-squares (PLS) regression approach is employed. In addition, a stepwise chain selection algorithm, originally developed for wavelength selection in spectroscopy, was employed for spatial selection purposes.[17] Through this spatial selection, an interpretation of the image-based Mueller matrices is provided, which sheds insight on the most relevant spatial positions and elements of the Mueller matrix. This step provides information on which elements of the Mueller matrix and the spatial information within the individual elements were used in the prediction of the particle-size-dependent scattering coefficient contributions.

2 Theory

2.1 Mueller Matrix/Stokes Vector Imaging

The polarization state for a given light field can be characterized by a Stokes vector, which is a 4×1 vector:[18]

$$
S = \begin{bmatrix} I \\ Q \\ U \\ V \end{bmatrix} = \begin{bmatrix} \langle E_x E_x^* \rangle_\tau + \langle E_y E_y^* \rangle_\tau \\ \langle E_x E_x^* \rangle_\tau - \langle E_y E_y^* \rangle_\tau \\ \langle E_x E_y^* \rangle_\tau + \langle E_y E_x^* \rangle_\tau \\ i(\langle E_x E_y^* \rangle_\tau - \langle E_y E_x^* \rangle_\tau) \end{bmatrix} \quad (1)
$$

where E_x and E_y are the electric field components parallel and perpendicular to a reference direction of light travel; I is the total light intensity; Q represents the tendency of the light to exhibit either horizontal or vertical linear polarization; U represents the tendency of the light to exhibit either +45° or −45° linear polarization; and V similarly represents the tendency of the light to exhibit either right or left circular polarization. The angle brackets, $\langle \ldots \rangle_\tau$, represent the time average over the temporal integration time, which can be assumed to be much greater than the optical period. Due to the temporal integration, the time dependence of the electric fields is suppressed. A Mueller matrix is a 4×4 matrix that describes how an incident Stokes vector, S_{inc}, is transformed by a given sample. In essence, the Mueller matrix can be thought of as an optical fingerprint of a sample. Therefore, if the Mueller matrix, M, is known for a sample, the output or resulting Stokes vector, S_{out}, is given by

$$
S_{\text{out}} = M S_{\text{inc}} \quad (2)
$$

If the Mueller matrix for a given sample is unknown, all 16 elements can be determined through the acquisition of 16, 36, or 49 intensity-based measurements corresponding to different combinations of input and output polarization states.[14,15,19,24]

In our investigation, the polarization dependencies of the backscattered light from complex turbid media, consisting of mixtures of polystyrene spheres of different sizes, are investigated through image-based Mueller matrix polarization measurements. In these measurements, each element of an acquired Mueller matrix is a two-dimensional image rather than consisting of a single point. An example of an image-based Mueller matrix for a turbid phantom is shown in Fig. 1, where the size of each element is $1.6 \text{ cm} \times 1.6 \text{ cm}$ and the image plane is taken at the surface of the sample. It should be noted that each element of the Mueller matrix corresponds to the same sample area; however, the observed differences represent different polarization dependencies as further described in Sec. 3.1.

2.2 Partial Least Squares

Partial least squares (PLS) is a method that generalizes and combines features from principal component analysis (PCA) and multiple regression.[17,20] PLS regression is based on the linear transition from a large number of original descriptors to a new variable space based on a small number of orthogonal factors (latent variables). In other words, factors are mutually independent (orthogonal) linear combinations of original descriptors. This method proves particularly useful when it is desired to predict a set of dependent variables Y from a large set of independent variables X (i.e., predictors). PLS regression searches from a set of latent variables that performs simultaneous decompositions of X and Y with the constraint that these latent variables describe the maximum covariance between X and Y. This is followed by a regression step where the decomposition of X is used to predict Y. In our investigation, PLS is used to form a calibration model around a set of Mueller matrix image-based data, which are then used to predict the scattering coefficient contribution as a function of particle size.

2.3 Feature Selection

Although PLS is suitable for full data-set analysis, variable or feature selection is a commonly used procedure to reduce the size of data sets as well as to improve the prediction performance in calibration and validation. The reasoning behind improved prediction is well-described in literature.[17,20–23] and is due to a variety of factors. One specific reason is that irrelevant and/or redundant variables can be identified and removed, therefore improving the signal-to-noise ratio as well as reducing the overall number of observations to avoid overfitting the multivariate models. After variable selection, predictive abilities are usually enhanced and the models are much simpler and more robust.

In terms of implementation, optimization techniques such as simulated annealing (SA) and genetic algorithms (GAs) have frequently been used.[20–23] In this investigation, we adopted a previously reported algorithm, known as "chain select," to optimize our calibration models and locate the most relevant variables used in prediction.[17] This method employs a stepwise selection approach to improve PLS prediction through the use of multiple chains of rankings using signal-to-noise ratio (SNR), $|\hat{\beta}_i / \hat{\sigma}_i|$, where $\hat{\beta}_i$ is the slope estimated from ordinary least-square regression of spatial intensities X at the ith frequency onto Y variables (scattering coefficient), and $\hat{\sigma}_i$ is the estimated standard deviation at the ith location. The algorithm begins by computing the spectral SNR followed by ranking the variables in decreasing order of SNR. This is the first ranking chain, from which the variables with the largest rank is used to generate the "estimated spatial image" as the product of the regression coefficient and Y. The
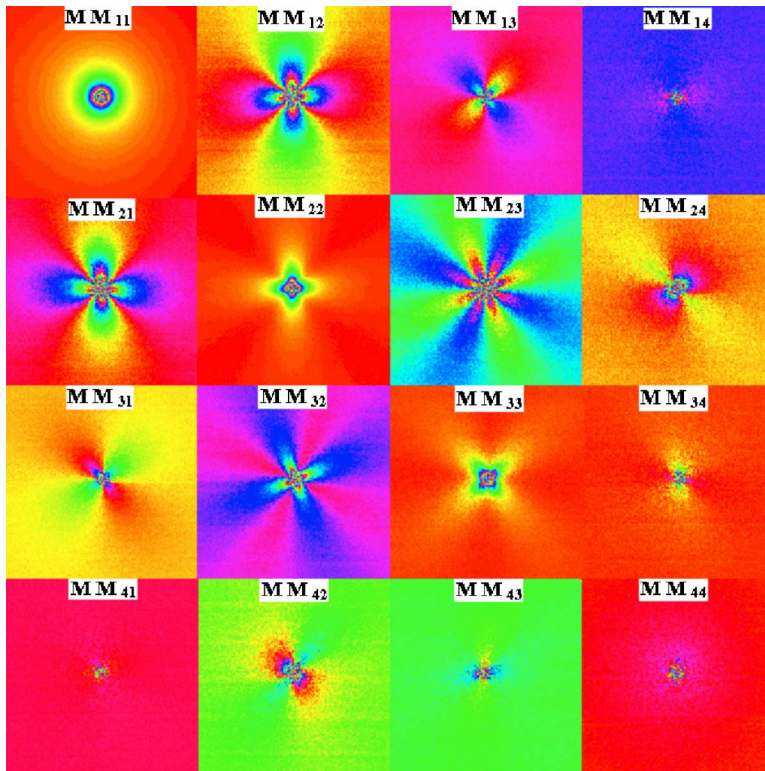
Fig. 1 An experimentally measured Mueller matrix for a complex polystyrene mixture consisting of 0.2, 0.5, 1, and 2 μm-diameter particles with respective scattering coefficient contributions of 0.5, 1.5, 0.25, and 5 cm^{-1} leading to an overall scattering coefficient of μ_s=7.25 cm^{-1}.

residual spatial images, which are calculated as the difference between the original image and the estimated image, are then used to calculate a second SNR. The second ranking chain is obtained by sorting the SNR in descending order. The process continues until a predetermined number of chains have been generated. Once the final ranking chain is generated, the evaluation phase that is common to most stepwise techniques begins. At each step, a variable is added, a calibration model is constructed, and the root-mean-square error of cross-validation (RMSECV) is generated. A spatial position is added to the selected positions only if it produces a reduction in RMSECV. In our case, the selected transformed 1-D spatial position arrays are then transformed back to get the 2-D spatial selections. As presented later, this algorithm provides considerable insight into how scattering type (e.g., Rayleigh versus Mie) and particle size are encoded into the Mueller matrix.

3 Materials and Methods

3.1 Experimental Setup

The experimental setup, seen in Fig. 2, is similar to that reported in our previous study.[25] An argon ion laser (Melles Griot, CA) is used as the light source, emitting at a wavelength of 514 nm with a power of 5.45 mW. The beam is initially polarized by a horizontal Glan Thompson polarizer (Melles Griot, CA). The input polarization state is controlled electro-optically with no moving parts via two liquid-crystal voltage-dependent variable retarders (Meadowlark Optics, CO) with the ability to alter the incident polarization state

between horizontal (H), vertical (V), +45° linear (P), and right circular (R). The polarized beam is then focused by a lens through a hole in a 45° mounted mirror onto the sample. The backscattered light from the sample is reflected through the output pathway consisting of two additional electro-optic variable retarders and a Glan–Thompson vertical polarizer. The output pathway is used to analyze the backscattered polarization state (e.g., H, V, P, R). The image is acquired by a thermoelectric-cooled 512×512 16-bit CCD camera (Apogee CCD, CA) fitted with a Nikon adjustable zoom lens. The sample Mueller matrix is calculated by 16 combinations of
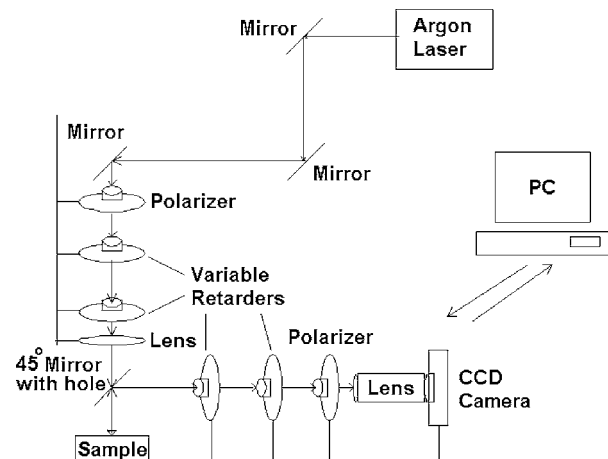
Fig. 2 Experimental Mueller matrix backscattering imaging system.

input and output polarization states. The Mueller matrix reconstruction is automated through a custom LabVIEW® program, which controls the CCD camera and the polarization states through a digital-to-analog (D/A) converter (National Instruments, Austin, TX).

3.2 Poly-Disperse Suspensions (Complex Mixtures)

Poly-disperse aqueous polystyrene sphere suspensions are used as the scattering phantoms, with each containing several particle sizes (0.2, 0.5, 1, and 2 μm-diameter spheres). Two sets of 60 30 ml phantoms with overall scattering coefficients ranging from 1 to 15 cm^{-1} were created with each containing two or more different sizes of polystyrene spheres. The overall scattering coefficient, for a given sample, consists of individual scattering coefficient contributions for each particle size, which were chosen through random combinations. Therefore, each sample consists of multiple particle sizes each in different concentrations. For example, one of the phantoms with an overall scattering coefficient of μ_s=7.25 cm^{-1} contained 0.2, 0.5, 1, and 2 μm-diameter particles each with an individual scattering coefficient contribution of 0.5, 1.5, 0.25, and 5 cm^{-1}, respectively.

3.3 Experimental Protocol

For each set of 60 poly-disperse turbid phantoms, the respective 16-element Mueller matrices were acquired. The individual matrix elements were cropped to 180×180 pixels, with the center located at the physical laser incidence point. The approximate size of each image was 1.6 cm $\times$ 1.6 cm. To illustrate the type of images acquired, Fig. 1 is an example of a Mueller matrix image collected for the previously described μ_s=7.25 cm^{-1} complex phantom. Due to the image symmetry observed in the individual elements, in order to reduce the data set, only the upper left quadrant of each element is taken into consideration in the analysis. In addition, all elements are normalized to the first element, M_{11}, and the other 15 elements except M_{11} are combined together into a single 2-D image array. To apply the PLS technique, the combined 2-D array for each of the 60 samples is transformed into a 1-D data array, resulting in 60 image spectra of length 121,500. All calculations were performed in MATLAB® 6.5 (Mathworks, Natick, MA) and with the PLS_Toolbox (Eigenvector Technologies, Manson, WA). For one set of data, a PLS calibration model was determined using a total of 5 latent variables. This number of latent variables was determined through a cross-validation analysis in which 5 latent variables minimized the cross-validation error. This approach ensures that the data set is not "overmodeled" during the calibration process. One possible explanation why five latent variables minimizes the cross-validation error is that 1 latent variable is needed to represent each particle size, 4 total, and an additional one for the variation in water concentration. The second set of data was used as an independent data set to perform validation. Respective standard errors of calibration and validation for prediction of each particle size were then computed.

In addition to the standard PLS analysis, previously described, a second calibration model was also formed after preprocessing the raw data set to identify the most relevant spatial positions, which were then used to resample the data to obtain a reduced data set. This was achieved via the "chain-select" algorithm discussed in Sec. 2.3. The purpose behind this step was two-fold: (1) to further reduce prediction error and the overall data size required for prediction, and (2) to identify the most relevant information present in the Mueller matrix structure that was used for accurate prediction for each respective particle size in a complex mixture. As with the prior analysis, respective standard errors of calibration and validation for prediction of each particle size were then computed.

4 Results and Discussion

According to the methods described in Sec. 3, a PLS multivariate calibration model was formed from one set of Mueller matrix raw data consisting of a total of 60 phantoms, each representing a poly-disperse mixture of polystyrene spheres of different size spheres. Five latent variables were utilized in the calibration model, which was chosen based on the total possible number of different size spheres present in a single sample, four total, plus an additional one for the variation in water concentration. The use of five latent variables allowed the capture of high variance in both the transformed image intensities and the scattering coefficient contributions, 90.15% and 90.64%, respectively, while avoiding overfitting of the model to the data. Plots of predicted versus actual scattering coefficient contribution for every particle size within each of the 60 samples in calibration using the raw data set (i.e., unprocessed for spatial selection) are presented in Fig. 3. The standard errors of calibration (SEC), summarized in the first column of Table 1, for each particle size ranged from 0.3308 to 0.8582 cm^{-1}. In addition, to further validate the predictive capability of the computed model, a second set of independently collected data was used. In validation, the prediction results of scattering coefficient contribution for each particle size are shown in Fig. 4 and summarized in the second column in Table 1. Although the standard errors of prediction (SEP) as compared to SECs are larger in each case, in comparison to the overall range of scattering coefficient contributions being predicted, it does not appear that the calibration model is significantly overfitting the data. As can be partially seen in Fig. 3, although many data points overlap, the respective prediction errors for 0.2, 0.5, 1, and 2 μm-diameter particles for zero concentration are 0.3144, 0.4238, 0.3381, and 0.3730 cm^{-1}, respectively. Based on this, the majority of the overall error contribution appears to be caused by prediction errors for the zero-contribution scattering coefficient (i.e., prediction error when a certain type of particle is not present in the sample). Therefore, signal and noise due to other particle sizes cannot completely be distinguished in the model.

As an additional processing step, the raw data used in the previously described analysis were preprocessed before computing the calibration model with the PLS technique. The purpose of the preprocessing was to determine the most useful spatial locations in the overall Mueller matrix that provides accurate prediction of the scattering coefficient contribution for each respective particle size in the poly-disperse suspensions. To perform the spatial selection preprocessing, the method described in Secs. 2.3 and 3.3 was employed. After preprocessing the raw data set, its overall size was reduced from 60 samples $\times$ 121,500, in length to 60 samples $\times$ 2,999,
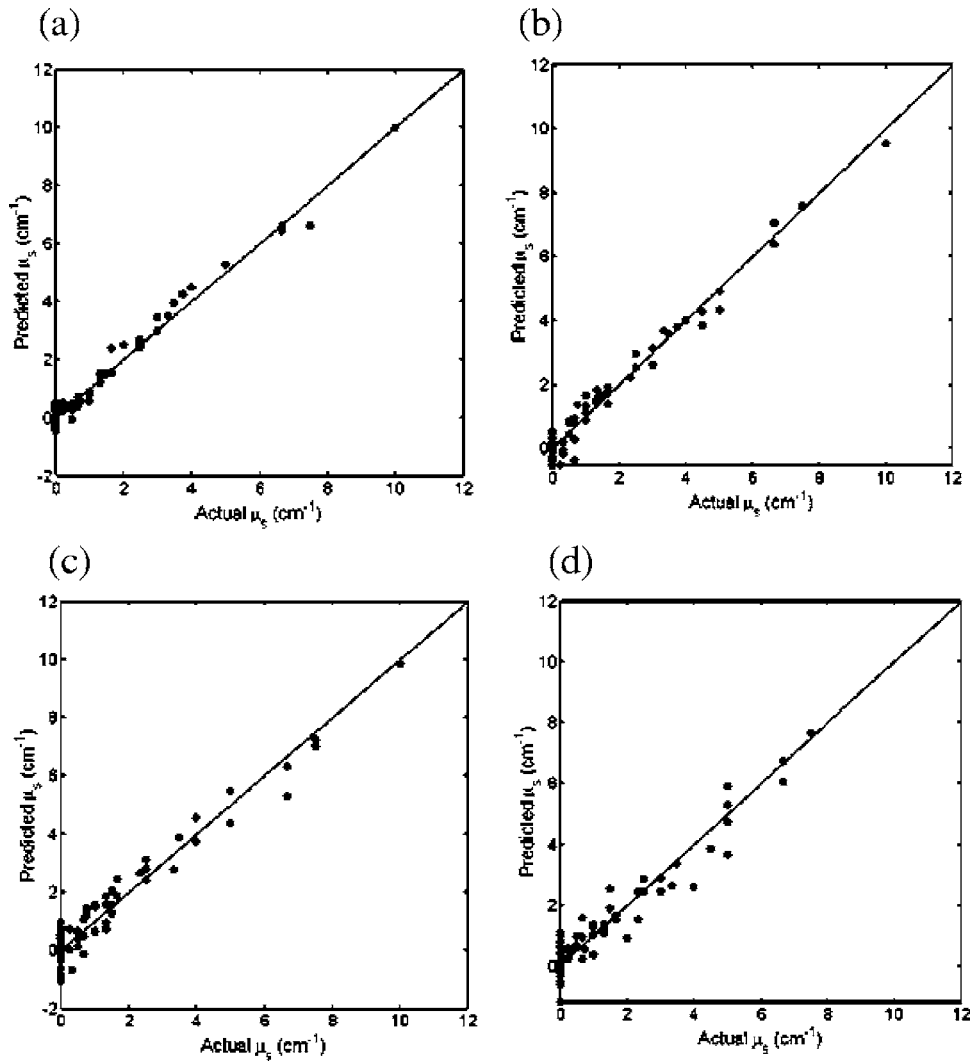
Fig. 3 Scattering coefficient contribution prediction in calibration for (a) 0.2 μm, (b) 0.5 μm, (c) 1.0 μm, and (d) 2.0 μm-diameter spheres.

in length. Using the resampled data set, we formed a PLS multivariate calibration model. Again, five latent variables were utilized in the calibration model. For the spatially selected preprocessed data, the standard errors of calibration (SEC), summarized in the third column of Table 1, for each particle size ranged from 0.1585 to 0.7372 cm^{-1} and the over-

all errors were reduced in comparison to the unprocessed raw data in all cases, except for the 1 μm-diameter spheres. In addition, to further validate the predictive capability of the computed model, the second set of independently collected data was resampled, choosing the same spatial locations used during calibration. In validation, the prediction results of scattering coefficient contribution for each particle size are summarized in fourth column of Table 1. As can be seen, similar standard errors of prediction (SEP) compared to the SEPs using the raw data set are observed; however, this was achieved using a considerably smaller subset of the original data size.

Although the use of spatial selection can considerably reduce the overall size of the data set needed for accurate prediction, it can also shed insight about the inherent structure of the data set and the location of relevant points useful in the prediction of the respective components (e.g., in this case, the scattering coefficient contribution for each respective particle size). In our experimental approach, the probing light has a wavelength of 514 nm, or 0.514 μm. For particle sizes significantly smaller than the wavelength of light, scattering with

Table 1 Scattering Coefficient Contribution SEC and SEP for (a) Full Data Set and (b) Spatially Selected Data Set (SEC and SEP Units: cm^{-1})

Particle	(a) Full data sets (raw data)		(b) After spatial selection	
	SEC	SEP	SEC	SEP
0.2 μm	0.3308	0.4514	0.1585	0.3571
0.5 μm	0.8582	0.9635	0.3539	0.7837
1 μm	0.5116	1.5237	0.7372	1.5619
2 μm	0.8041	0.9877	0.5648	0.9138

(a)

(b)

(c)

(d)
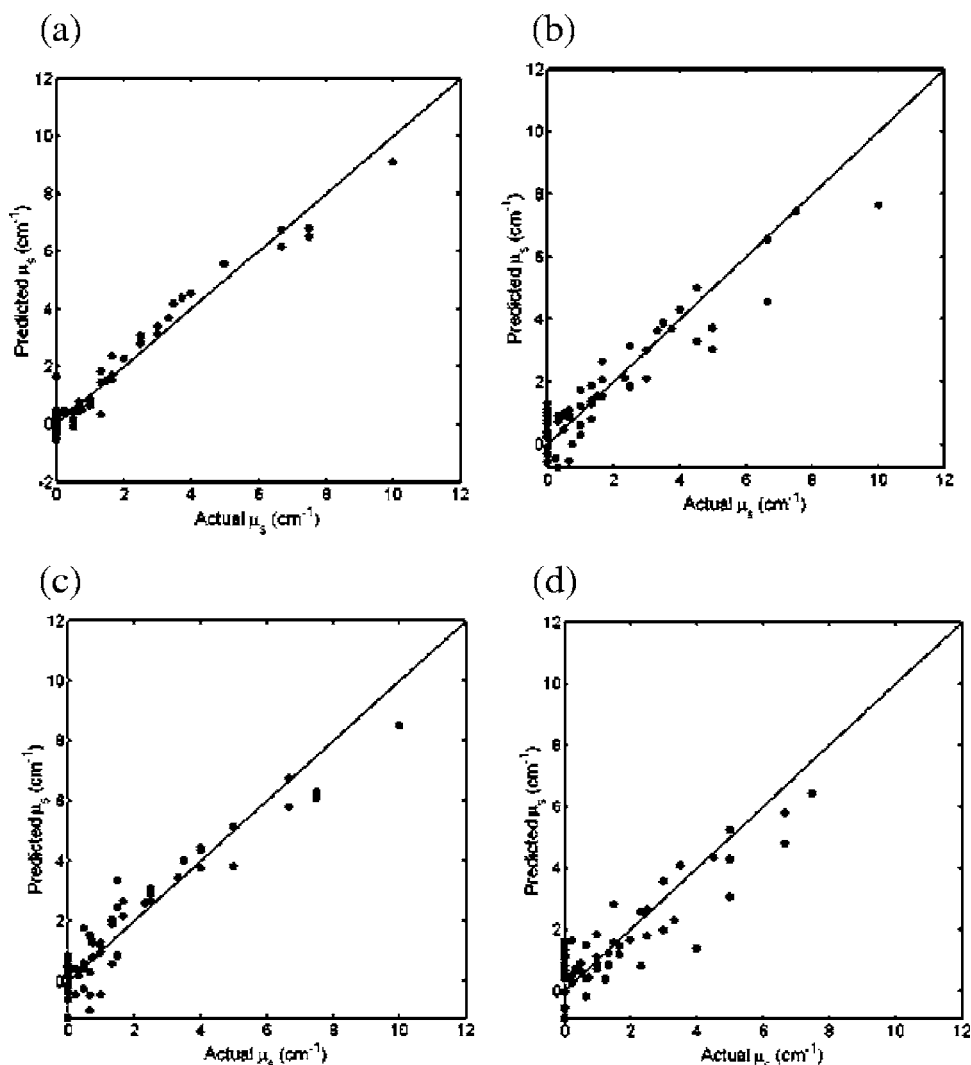
Fig. 4 Scattering coefficient contribution prediction in validation for (a) 0.2 μm, (b) 0.5 μm, (c) 1.0 μm, and (d) 2.0 μm-diameter spheres.

properties as characterized by the Rayleigh approximation is more dominant; for particle sizes greater than the wavelength of light, scattering with properties as characterized by Mie theory is more dominant. Through the use of the employed spatial selection method, we can show that the type of scattering involved is directly encoded within specific areas of the Mueller matrix for each respective particle size. To illustrate this, the Mueller element M_{12} was chosen (see Fig. 5). In the M_{12} element, it can be seen for the 0.2 μm particle size, Fig. 5(a), where Rayleigh scattering was dominant, considerable locations near the center of the element were used in prediction. In addition, locations to represent or preserve the azimuthal variations in the element were also selected. As the particle size begins to approach the wavelength of light (e.g., for the 0.5 μm particle size), as shown in Fig. 5(b), several locations throughout the M_{12} element were chosen, although there is less information chosen to preserve the azimuthal variations. For particles sizes greater than the wavelength of light (e.g., for the 1 μm and 2 μm particle sizes) where Mie scattering dominates, less information was chosen near the center of the element and more information along the +45°

and 135° angles increasing toward the outer boundary of the element was chosen. Therefore, this is indicative of how the scattering type is encoded within the Mueller matrix. Similarly, results were seen to a lesser degree for other specific elements in the Mueller matrix as well. Other information, such as particle shape, would be expected to be encoded in the Mueller matrix in a similar fashion and will be the focus of future investigations.

5 Conclusion

By the use of backscattered polarized light imaging in turbid media, we have shown, in part, how variations in image-based Mueller matrices encode information on the scattering type, particle size, and particle concentration. Furthermore, methods such as the PLS technique can be employed in the formation of mathematical models to quantitatively predict scattering coefficient contributions as a function of particle size. In future investigations, further extensions to improve the robustness of such modeling approaches to handle increasingly complex media such as those with non-uniform spatial distri-
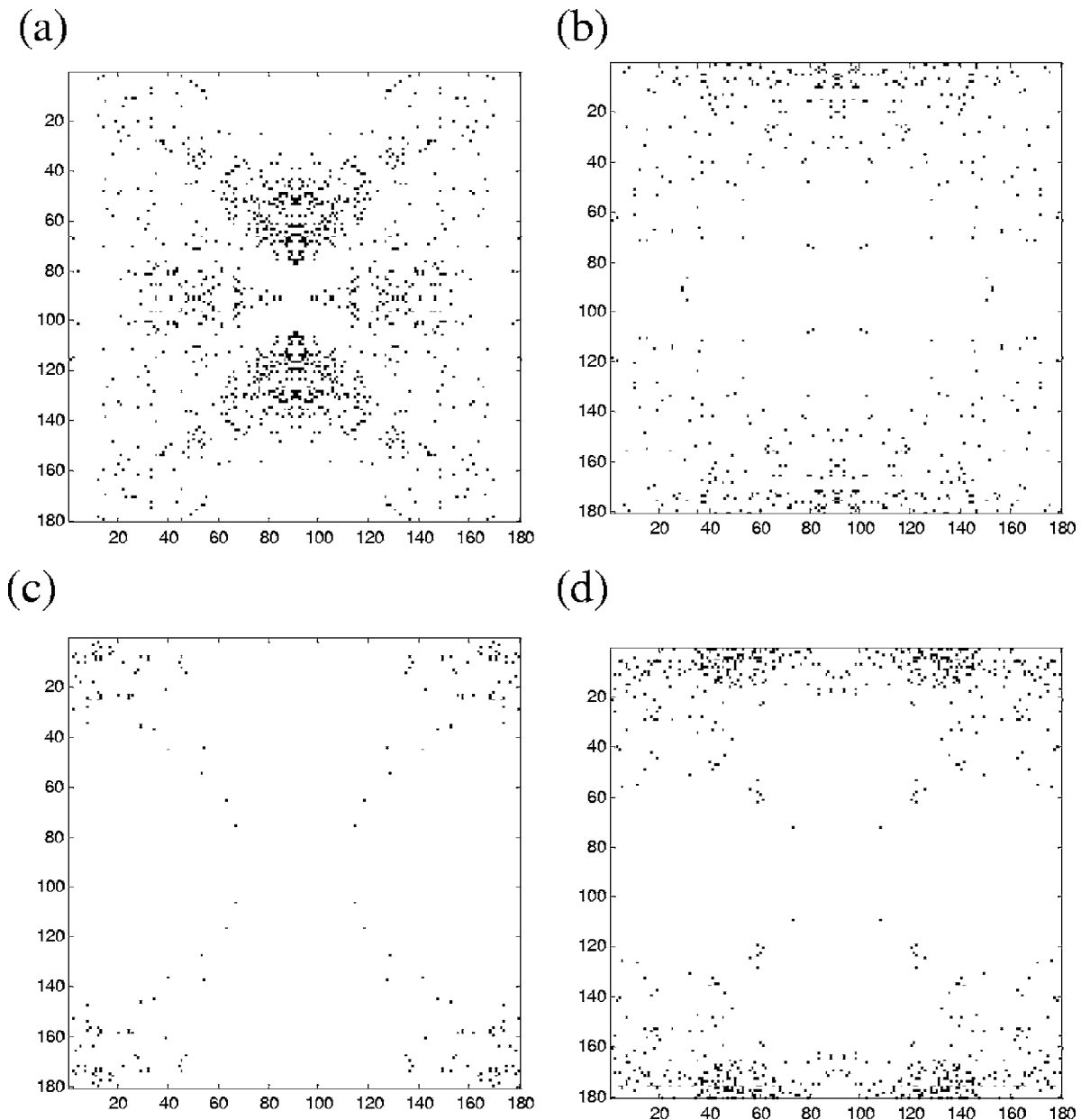
Fig. 5 Spatial selection results for the M_{12} element. Dots indicate points in the M_{12} element that were chosen to predict the scattering coefficient contribution for (a) 0.2 μm, (b) 0.5 μm, (c) 1.0 μm, and (d) 2.0 μm-diameter spheres.

butions and differing particle geometries may eventually allow such methods to be potentially used as a diagnostic tool to distinguish between tissue types and abnormalities that have differences in cellular structures and tissue components.

References

1. W. S. Bickel, J. F. Davidson, D. R. Huffman, and R. Kilkson, "Application of polarization effects in light scattering: A new biophysical tool," *Proc. Natl. Acad. Sci. U.S.A.* **73**, 486–490 (1976).
2. A. H. Hielscher, J. R. Mourant, and I. J. Bigio, "Influence of particle size and concentration on the diffuse backscattering of polarized light from tissue phantoms and biological cell suspensions," *Appl. Opt.* **36**(1), 125–135 (1997).
3. V. Backman, R. Gurjar, K. Badizadegan, I. Itzkan, R. R. Dasari, L. T. Perelman, and M. S. Feld, "Polarized light scattering spectroscopy for quantitative measurement of epithelial cellular structures in situ,"
IEEE J. Sel. Top. Quantum Electron. **5**, 1019–1026 (1999).
4. M. Bartlett and H. B. Jiang, "Measurement of particle size distribution in multilayered skin phantoms using polarized light spectroscopy," *Phys. Rev. E* **65**(3), 31906-1-8 (2002).
5. S. G. Demos and R. R. Alfano, "Optical polarization imaging," *Appl. Opt.* **36**(1), 150–155 (1997).
6. S. L. Jacques, J. R. Roman, and K. Lee, "Imaging superficial tissues with polarized light," *Lasers Surg. Med.* **26**, 119–129 (2000).
7. A. N. Yaroslavsky, V. Neel, and R. R. Anderson, "Optical mapping of non-melanoma skin cancer," *Prog. in Biom. Opt. and Imag.* **5**(15), 60–63 (2004).
8. O. V. Angelsky, A. G. Ushenko, and Y. G. Ushenko, "Investigation of the correlation structure of biological tissue polarization images during the diagnostics of their oncological changes," *Phys. Med. Biol.* **50**(20), 4811–4822 (2005).
9. J. W. Pickering, S. Prahl, N. van Wieringen, J. Beek, H. Sterenborg, and M. Germert, "Determining the optical properties of turbid media by using the adding-doubling method," *Appl. Opt.* **32**(4), 399–410

(1993).

10. L. V. Wang and S. L. Jacques, "Use of a laser beam with an oblique angle of incidence to measure the reduced scattering coefficient of a turbid medium," *Appl. Opt.* **34**(13), 2362–2366 (1995).

11. F. Bevilacqua, D. Piguet, P. Marquet, J. D. Gross, B. J. Tromberg, and C. Depeursinge, "In vivo local determination of tissue optical properties," *Proc. SPIE* **3194**, 262–268 (1997).

12. F. Bevilacqua, D. Piguet, P. Marquet, J. D. Gross, D. Jeffrey, D. Jakubowski, V. Venugopalan, B. J. Tromberg, and C. Depeursinge, "Superficial tissue optical property determination using spatially resolved measurements close to the source: Comparison with frequency domain photon migration measurements," *Proc. SPIE* **3597**, 540–547 (1999).

13. P. Thueler, I. Charvet, F. Bevilacqua, P. Marquet, P. Meda, B. Vermeulen, C. Depeursinge, M. St. Ghislain, and G. Ory, "In vivo endoscopic tissue diagnostics based on spectroscopic absorption, scattering, and phase function properties," *J. Biomed. Opt.* **8**(3), 495–503 (2003).

14. W. S. Bickel and W. M. Bailey, "Stokes vectors, Mueller matrices, and polarized scattered light," *Am. J. Phys.* **53**, 468–478 (1985).

15. W. S. Bickel, A. J. Watkins, and G. Videen, "The light-scattering Mueller matrix elements for Rayleigh, Rayleigh–Gans, and Mie spheres," *Am. J. Phys.* **55**(6), 559–561 (1987).

16. H. C. van de Hulst, *Light Scattering by Small Particles* John Wiley & Sons, New York (1957).

17. M. J. McShane, B. D. Cameron, M. Motamedi, G. Cote, and C. Spiegelman, "A novel peak-hopping stepwise feature selection method with application to Raman spectroscopy," *Anal. Chim. Acta* **388** 251–264 (1999).

18. R. M. Azzam and N. M. Bashara, *Ellipsometry and Polarized Light*, Elsevier, Amsterdam, (1987), pp. 490–492.

19. J. S. Baba, J. Chung, A. H. DeLaughter, B. D. Cameron, and G. L. Coté, "Development and calibration of an automated Mueller matrix polarization imaging system," *J. Biomed. Opt.* **7**, 341–349 (2002).

20. D. Broadhurst, R. Goodacre, A. Jones, J. Rowland, and D. Kee, "Genetic algorithms as a method for variable selection in multiple linear regression and partial least squares regression, with applications to pyrolysis mass spectrometry," *Anal. Chim. Acta* **348**, 71–86 (1997).

21. S. Osborne, R. Jordan, and R. Keunnemeyer, "Method of wavelength selection for partial least squares," *Analyst (Cambridge, U.K.)* **122** 1531–1597 (1997).

22. R. Leardi, "Application of genetic algorithm-PLS for feature selection in spectral data sets," *J. Chemom.* **14**, 643–655 (2000).

23. U. Horchner and J. H. Kalivas, "Further investigation on a comparative study of simulated annealing and genetic algorithm for wavelength selection," *Anal. Chim. Acta* **311**,1–13 (1995).

24. B. D. Cameron, M. J. Rakovic, M. Mehrubeoglu, G. W. Kattawar, S. Rastegar, L. V. Wang, and G. L. Coté, "Measurement and calculation of the two-dimensional backscattering Mueller matrix of a turbid medium," *Opt. Lett.* **23**(7), 485–487 (1998).

25. A. Nezhuvingal, Y. Li, H. Anumula, and B. D. Cameron, "Mueller matrix optical imaging with application to tissue diagnostics," *Proc. SPIE* **4961**, 137–146 (2003).